The Astrophysical Journal, 830:58 (13pp), 2016 October 20 doi:10.3847/0004-637X/830/2/58

DETERMINATION OF CORONAL MASS EJECTION PHYSICAL PARAMETERS FROM A COMBINATION OF POLARIZED VISIBLE LIGHT AND UV Lyα OBSERVATIONS

R. Susino and A. Bemporad
Istituto Nazionale di Astrofisica (INAF), Osservatorio Astrofisico di Torino, Via Osservatorio 20, I-10025 Pino Torinese, Torino, Italy
Received 2016 June 30; revised 2016 July 27; accepted 2016 July 30; published 2016 October 11

ABSTRACT

Visible-light observations of Coronal Mass Ejections (CMEs) performed with coronagraphs and heliospheric imagers (in primis on board the *Solar and Heliospheric Observatory* and *STEREO* missions) have offered the best way to study the kinematics and geometrical structure of these fundamental events so far. Nevertheless, it has been widely demonstrated that only combination of multi-wavelength data (including X-ray spectra, EUV images, EUV-UV spectra, and radio dynamic spectra) can provide complete information on the plasma temperature and density distributions, non-thermal motions, magnetic fields, and other physical parameters, for both CMEs and CME-related phenomena. In this work, we analyze three CMEs by combining simultaneous data acquired in the polarized visible light by the LASCO-C2 coronagraph and in the UV H I Lyα line (1216 Å) by the UVCS spectrometer, in order to estimate the CME plasma electron density (using the polarization-ratio technique to infer the 3D structure of the CME) and temperature (from the comparison between the expected and measured Lyα intensities) along the UVCS field of view. This analysis is primarily aimed at testing the diagnostic methods that will be applied to coronagraphic observations of CMEs delivered by the Metis instrument on board the next ESA-Solar Orbiter mission. We find that CME cores are usually associated with cooler plasma ($T \sim 10^6$ K), and that a significant increase of the electron temperatures is observed from the core to the front of the CME (where $T > 10^{6.3}$ K), which seems to be correlated, in all cases, with the morphological structure of the CME as derived from visible-light images.

Key words: Sun: corona – Sun: coronal mass ejections (CMEs) – Sun: UV radiation

1. INTRODUCTION

During major solar eruptions (or Coronal Mass Ejections—CMEs), huge bubbles of highly ionized plasma (often associated with shock waves and Solar Energetic Particles—SEPs) expand into the interplanetary space, affecting a significant fraction of the whole heliosphere, and eventually propagating even out of the heliopause as interstellar shocks in the most dramatic cases, as recently reported with *Voyager 1* observations (Gurnett et al. 2015). Solar transients (flares, CMEs, and prominence eruptions) have an impact on all the planetary objects, interacting with their magnetospheres or magnetospheric-like structures and inducing geomagnetic storms (see the review by Akasofu 2011), as well as beautiful auroras on Earth and other planets (Hultqwist 2008). These events likely played a role even in the development of life on Earth, for instance by modulating the rate of galactic cosmic rays impacting the early Earth's atmosphere (via the well-known "Forbush decrease" effect; see Lockwood 1971) and on the atmospheric chemistry (Airapetian & Usmanov 2016). Moreover, the study of these events is very important also from a theoretical point of view, because in order to understand their origin and interplanetary evolution it is necessary to consider many different plasma physical processes (such as plasma instabilities, magnetic reconnections, wave-particle interactions, etc.), that are only partially understood.

From the observational point of view, the study of solar eruptions can be performed using many different data delivered daily by both ground- and space-based observatories. Nevertheless, images of the solar disk can provide only information on the location of the source region, on the eruption start time, and on the early expansion phases. Then, after the eruptions take off and leave the Sun, their subsequent evolution can be followed only with two classes of instruments: space-based coronagraphs and heliospheric imagers that are the only instruments covering the huge amount of space traveled by solar eruptions during their propagation from the Sun to the Earth and beyond. Without data provided by space-based coronagraphs and heliospheric imagers it would be simply impossible to characterize the real CME propagation angle and CME speed, and to investigate the physical processes occurring during their interplanetary propagation.

It is well known today that, after the main impulsive acceleration phase occurring in the lower corona, solar eruptions are subject to many different processes affecting their evolution, which is never like a simple radial and self-similar expansion. During their early propagation phases, CMEs are often channelled by coronal streamers and/or deflected away from nearby coronal holes (see Möstl et al. 2015 and references therein), or toward the interplanetary current sheet (e.g., Byrne et al. 2010; Isavnin et al. 2014); these interactions may modify their propagation directions up to 25° with respect to the location of the source region (Kay et al. 2013), influencing the strength of the eventual impact on Earth. Significant rotations of CMEs around their propagation axis are also observed in many cases (e.g., Bemporad et al. 2011; Thompson et al. 2012), which change the orientation of the magnetic field of the associated magnetic cloud impacting the Earth's magnetosphere, and in turn their capability to induce geomagnetic storms. Moreover, significant magnetic drag occurs during the interplanetary propagation of CMEs, leading to further accelerations or decelerations of the ejecta (depending on the expansion speed relative to the ambient solar wind) that affect the expected arrival times at Earth (e.g., Temmer et al. 2011; Iju et al. 2014). Furthermore, when multiple eruptive events are ejected in sequence, CME–CME

interactions may occur, increasing their final geoeffectiveness (see Farrugia et al. 2006; Wu et al. 2007).

All these phenomena make CME observations by coronagraphs and heliospheric imagers crucial for understanding these events and forecasting their impact on the Earth. Moreover, previous experience with visible-light (VL) coronagraphs shows that unique information can be derived only when data acquired at different wavelengths are combined together, i.e., not only images in the VL, but also X-ray spectra, EUV images, EUV-UV spectra, and radio dynamic spectra. In particular, the combination of observations acquired in the VL by different coronagraphs and in the UV spectral range by the UVCS spectrometer (Kohl et al. 1995) on the *Solar and Heliospheric Observatory* (*SOHO*), allowed us to characterize the distribution of plasma temperatures (electron and ion) and their evolution inside the CME core and front, to study many CME-related phenomena, such as post-CME current sheets and CME-driven shocks, and to reveal the three-dimensional (3D) CME structure (see Kohl et al. 2006 for an extensive review of these results). More recently, UVCS spectra have been combined for the first time with *SOHO* and *STEREO* VL images to perform the first stereoscopic and spectroscopic reconstruction of a CME (Susino et al. 2014), to derive the physical parameters of coronal plasma—including the magnetic field—across CME-driven shocks (e.g., Bemporad et al. 2014; Susino et al. 2015), and to derive kinetic temperature, gas pressure, and filling factor in erupting prominences (Heinzel et al. 2016). All of these works demonstrate the importance of complementarity of VL and UV observations of solar eruptions.

In the near future, combined VL and UV images will be provided by the Metis coronagraph (Antonucci et al. 2012; Fineschi et al. 2012) on board the ESA-Solar Orbiter mission, due to launch in 2018 October. The Metis instrument will acquire the first-ever simultaneous observations of the solar corona in the polarized visible light (broadband 580–640 nm) and in the UV (narrowband around the H I Lyα 1216 Å line), even if, since 2012, the instrument has lost its spectroscopic capabilities. The aim of the present work is to perform the first tests on the diagnostic capabilities for CMEs that will be possible with future Metis data. This test is performed here using available simultaneous observations of real CMEs acquired in the polarized visible light by the *SOHO*/LASCO-C2 coronagraph (Brueckner et al. 1995) and in the UV by the UVCS spectrometer. Because the Metis coronagraph will not provide spectroscopic observations, in this work, we focused only on the observed evolution of UV Lyα intensities, simulating the information that will be provided by Metis. The paper is organized as follows: after a description of the selected events and data sets (Section 2), we describe the diagnostics (Section 3) we applied for the determination of CME electron density (Section 3.1) and electron temperature (Section 3.2), and then we discuss our results (Sections 4 and 5).

2. OBSERVATIONS

For the purpose of this work, we looked for CME events for which simultaneous measurements of visible-light polarized brightness (*pB*) by LASCO-C2 and H I Lyα spectra by UVCS were available.

In order to find suitable events, we first searched the LASCO CME catalog for all the CMEs observed with LASCO-C2 during the acquisition of a polarimetric sequence for the measurements of the *pB*; then we made a cross-search of the UVCS observation logs to narrow down the list of the possible candidates to the events that were simultaneously observed by UVCS, selecting only those where a significant part of the CME structure crossed the UVCS field of view (FOV). The probability to have good candidates is quite low, mostly because, on the one hand, LASCO-C2 acquires only one or two polarimetric sequences per day, i.e., with a very poor cadence, on the other hand, UVCS detectors have become progressively more and more degraded since the year 2006, with reduced FOV. Moreover, for a large amount of time UVCS observations were performed with the slit centered at projected altitudes below the inner edge of the LASCO-C2 occulter (~2.2 solar radii), thus preventing the possibility to analyze erupting events at the same location and at the same time with the two instruments. As a result, only three events in the whole *SOHO* era were found. All three selected CMEs consist of minor events with small plasma eruptions at quite low velocities, as we will describe in the following.

2.1. Description of the Events

In the event of 2000 November 8 (hereafter Event 1), which is classified as a narrow (angular width of ~59°), slow CME, the CME leading edge entered in the LASCO-C2 FOV at 19:27 UT with an estimated plane-of-the-sky (POS) speed of ~160 km s^{-1}. The CME was associated with a prominence eruption and propagated in the southeast quadrant at a latitude of ~30°S showing the classical, quite symmetrical three-part structure (see Figure 1, top row). The CME launch time, derived by extrapolating the LASCO-C2 measurements to the projected height of 1 $R_\odot$, was approximately at 17:19 UT, in agreement with MLSO/Mark-IV image sequences (Figure 2). LASCO-C2 acquired a polarimetric sequence for the measurement of the polarized visible light between 20:59 and 21:03 UT. *SOHO*/EIT 304 and 195 Å images show that the CME probably originated from active region (AR) NOAA 09227 (located at 10°S 55°E): prominence material laying above the source AR appears to be ejected between 13:19 UT and 19:19 UT, as showed by the only two EIT 304 Å images available before and after the estimated CME launch time. The eruption is barely visible in corresponding EIT 195 Å images, where a weak evacuation of plasma followed by a rearrangement of the magnetic configuration above the source AR can be noticed. Although an M2.9 class flare was detected by the *GOES* satellite at 16.30 UT—i.e., very close to the CME start time—this flare occurred at the NE limb, as shown by TRACE images.

The event of 2000 December 25 (hereafter Event 2) consists of a small-scale eruption of plasma along a coronal streamer triggered by an adjacent CME (see Bemporad et al. 2010, for similar CME-induced eruptions). The coronal configuration above the NE limb before the event was characterized by the presence of a faint, quite stable streamer located at a latitude of ~60°N as shown by the LASCO-C2 white-light images. The first sign of ejection appeared in the LASCO-C2 FOV at 18:54 UT as a brightening at the visible base of the streamer; the emerging plasma "blob" later on traveled along the streamer with an estimated velocity of ~250 km s^{-1} showing a complex configuration with evidence of a small-scale filamentary structure (see Figure 1, middle row). The ejection start time, as extrapolated from the LASCO height-time

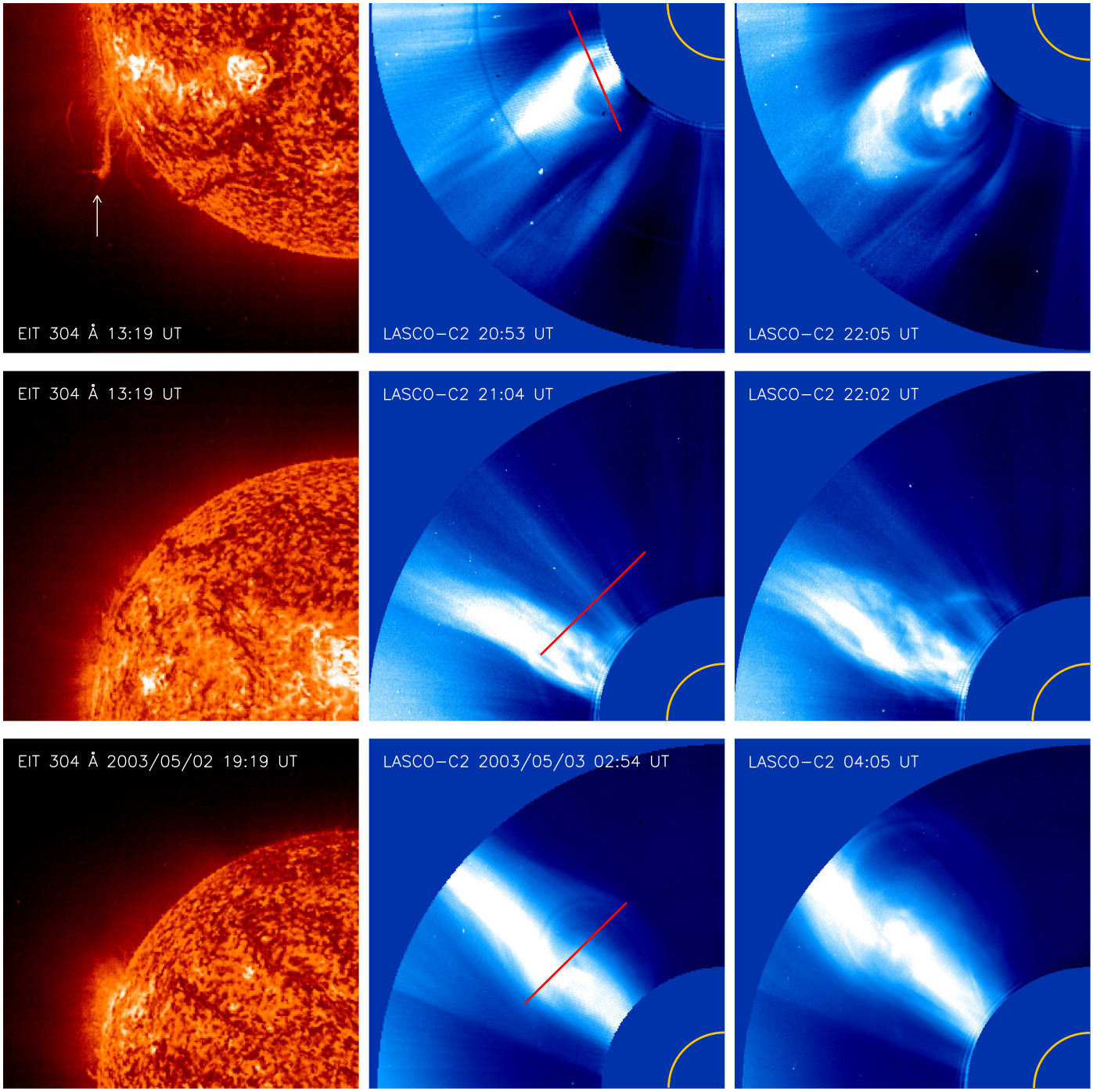

Figure 1. Left column: *SOHO*/EIT 304 Å images acquired before the CMEs occurred on 2000 November 8 (top row), 2000 December 25 (middle row), and 2003 May 2–3 (bottom row). Middle and right columns: LASCO-C2 total-brightness images (processed with the NRGF in order to better highlight the CME structure) at the time of the *pB* measurement and several hours later, respectively, showing the evolution of the three CMEs in the coronagraph field of view. In the middle column, the *SOHO*/UVCS field of view (the slit, represented as a red line) is also superimposed to mark the portion of the solar corona sampled by the spectrometer during the transit of the CME.

diagrams, was at 17:34 UT. The polarimetric sequence for the measurement of the *pB* was acquired between 20:52 and 21:00 UT. At 21:04 UT, when the leading edge of the ejected material was above $\sim$4.5 $R_{\odot}$, the hemispherical front of a faint CME entered the LASCO-C2 FOV propagating slightly northward to the streamer, at a latitude of $\sim$52°N, with approximately the same speed (as reported in the LASCO CME catalog). As the CME progressed, no clear signature of a bright core inside was detected in white light. EIT 195 and 304 Å images show little evidence of an eruption that occurred above the NE limb starting around 17:00 UT, quite consistent with the successive appearance of ejected plasma as seen by LASCO. The eruption is not associated with flares or EUV brightenings on the disk, hence the source region was most likely located behind the visible disk.

In the event of 2003 May 2–3 (hereafter Event 3), the first appearance of the CME leading edge in the LASCO-C2 FOV was at 23:50 UT on May 2. The initial velocity, estimated from

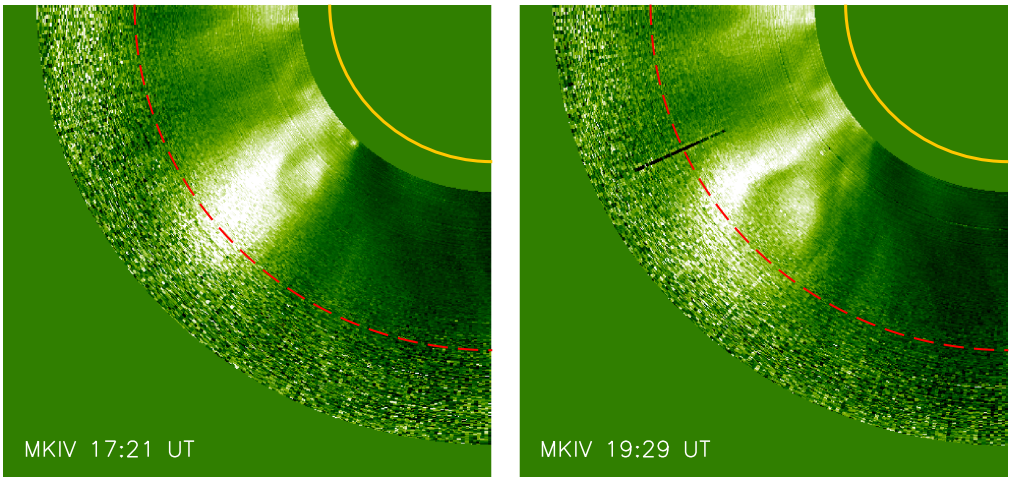

Figure 2. Mauna Loa Mark-IV visible-light images of the inner corona (processed with the NRGF) showing the initial evolution of Event 1. The red, dashed line marks the inner edge of the LASCO-C2 field of view (at 2.2 $R_\odot$). Note the clear three-part structure of the CME with the bright core, the dark void, and the almost hemispherical front surrounding it.

Table 1
Summary of UVCS Observations

Event	Date	Time[a]	Altitude Range ($R_\odot$)	PA (degree)	ρ[b] ($R_\odot$)	t_{exp}[c] (s)	Projected Slit Width (arcsec)	Spatial Bin Size (arcsec)
1	2000 Nov 08	18:02 UT	1.5–4.0	113	2.5	300	28	42
2	2000 Dec 25	20:58 UT	1.6–3.0[d]	45	3.0	120	42	21
3	2003 May 02	02:48 UT	1.6–3.5[d]	45	3.5	120	42	21

Notes.
[a] Initial time of UVCS observations.
[b] Heliocentric distance of the UVCS slit at the time of LASCO-C2 *pB* measurement.
[c] Exposure time.
[d] For this event, the radial scan was performed from higher to lower heights.

a second-order polynomial fit, was ~100 km s^{-1}. The CME propagated inside a large and bright mid-latitude coronal streamer at the latitude of ~45°N and exhibited a three-part structure with a faint hemispherical front and clear evidence of an inner core (see Figure 1, bottom row). At 02:58 UT LASCO-C2 started to acquire the sequence of three polarimetric images for the measurement of the *pB*, until 03:03 UT. At that time, the CME front velocity was around ~220 km s^{-1}. EIT 304/195 Å images did not show remarkable phenomena occurring below the coronal region where the CME propagated, and the ejection was not associated with a disk event; therefore, it most likely originated on the back side of the Sun, probably from ARs 10354/10355, which became visible at the NE limb in EIT 195 Å images on May 4.

2.2. UVCS Data

During the three events considered here, the UVCS FOV (a 42 arcmin long slit) performed a radial scan of the coronal region crossed by the CME. Details about the observations are listed in Table 1. Aside from the date and time, we report the radial scan altitude range, the polar angle (PA, measured counter-clockwise from north pole) where the slit was centered, the projected altitude of the slit (ρ) at the time of the *pB* measurement made by LASCO, the exposure time for each spectrum, the projected slit width, and the spatial bin size. In all cases, the detected spectral range includes the H I Lyα λ1215.6 Å line (acquired using the redundant path of the O VI channel with spectral binning of 2 pixels ≃0.1830 Å), the O VI $\lambda\lambda$ 1031.9/1037.6 Å doublet lines (acquired with spectral binning of 1 pixel ≃ 0.0991 Å for Events 1 and 2 pixels ≃ 0.1983 Å for Events 2 and 3), and other minor lines (not considered in this work). Standard calibration and data reduction was made with the latest version available of the UVCS Data Analysis Software (DAS 51).

In what follows, our analysis focuses on the H I Lyα intensities and profiles. For each event, we averaged the two exposures acquired around the time of the LASCO *pB* measurement, in order to increase the signal-to-noise ratio; for Events 2 and 3, we also averaged the data over two spatial bins (=42 arcsec). We then fitted a single Gaussian to the observed Lyα spectrum at each position along the slit, getting line intensities and widths. Usually spectra in the optically thin corona must be corrected for the ambient-corona contribution before spectral integration, in order to isolate the CME emission with respect to the emission of the surrounding corona aligned with the CME along the same line of sight. However, in all three cases, observations by UVCS started when the CME was already crossing the instrument FOV, making it impossible to get a reliable pre-event Lyα spectrum to be subtracted from the CME exposures to remove the quiet-corona contribution. To account for that, after integration of the Lyα spectra, we modeled the quiet-corona intensity at each position along the slit using a power-law extrapolation (with a $r^{-\alpha}$ dependence on the heliocentric distance), constraining the fit to the intensity measured in the slit regions not crossed by

the CME. The intensity from the fit extrapolated at the spatial region crossed by the CME was thus subtracted from the measured one.

The line widths $\Delta\lambda_{1/e}$ obtained from the Gaussian fit to the Lyα line profiles were corrected for the instrumental profile broadening and converted into effective temperatures with the usual relationship

$$\Delta\lambda_{1/e} = \frac{\lambda_0}{c}\sqrt{\frac{2k_{\rm B}T_{\rm eff}}{m_{\rm H}}}, \quad (1)$$

where λ_0 is the spectral line central wavelength at rest, c is the light speed, $k_{\rm B}$ is the Boltzmann constant, $m_{\rm H}$ is the hydrogen mass, and $T_{\rm eff}$ is the so-called effective temperature. Note that the observed profiles are likely broadened by non-thermal motions as well as by the line-of-sight component of the plasma bulk velocity; moreover, since we were not able to subtract a pre-event spectrum, they include a component relevant to the quiet corona as well. For these reasons, the derived effective temperatures are only an upper-limit estimate of the real hydrogen kinetic temperature.

The additional analysis of the O VI $\lambda\lambda$1032/1037 Å doublet lines detected by UVCS could, in principle, provide further information on the CME plasma outflow velocity. In fact, the O VI intensity ratio, $R = I_{1032}/I_{1037}$, is sensitive to the radial component of the plasma outward speed through the Doppler-dimming effect (see, e.g., Noci et al. 1987); the outflow velocity can be thus inferred from the comparison of the measured ratios with those predicted by models. In general, values of $R \gtrsim 2$ imply outflow velocities around or lower than 100 km s^{-1}, while at higher speeds, above $\sim$150 km s^{-1}, pumping of the O VI λ1037 Å by the C II $\lambda\lambda$1036/1037 Å lines causes R to be lower than two (see, e.g., Raymond & Ciaravella 2004; Ciaravella et al. 2005). Moreover, the dependence of R on the outflow velocity is a function of the electron density and temperature (see Dobrzycka et al. 2003).

Nevertheless, two reasons led us to neglect results based on the analysis of the O VI line ratios. First, the uncertainties on the O VI line intensities are larger than those affecting the Lyα line intensity, due to lower count statistics; moreover, since we were not able to correctly evaluate the coronal background intensity, we have larger uncertainties in the measurement of R (of the order of $\sim$30% for Event 1 and $\sim$50% for Events 2 and 3). The consequence is that in all the three cases, the intensity ratio does not differ significantly from 2 in most of the UVCS FOV (according to Raymond & Ciaravella 2004, we considered as statistically significant only departures of the ratio from the value of 2 larger than 2σ). Second, as we will discuss in the next sections, the analysis of the white-light emission measured by LASCO-C2 provided electron densities that are of the order or larger than 10^6 cm^{-3} in all cases. As clearly demonstrated by Dobrzycka et al. (2003) (for the 1999 April 15 CME at 1.98 $R_\odot$), the O VI intensity ratio at typical coronal temperatures and for electron densities higher than 10^6 cm^{-3} is $R \simeq 2$ in a wide range of velocities, so that it is impossible to identify a unique value for the CME outflow speed owing to those conditions. Therefore, we could not place reliable constraints on this parameter using these results and we preferred to estimate the outflow plasma velocity using the analysis of the CME dynamics in LASCO-C2 VL images (see below).

3. DIAGNOSTIC METHODS

3.1. Density Diagnostics from Polarized Visible Light

The coronal visible light (K-corona) is produced by the Thomson scattering of the photospheric incident radiation off coronal free electrons; VL images can provide the electron column density $N_e = \int_{\rm los} n_e\, dz$ using the method described, for instance, by Vourlidas et al. (2000): the number of scattering electrons along the LOS (i.e., the column density N_e, in units of cm^{-2}) is given by the ratio of the observed total brightness B over the brightness $B_{\rm exp}(z)$ expected for a single electron located at distance z from the plane of the sky. Usually this computation is done pixel-by-pixel in the CME exposure under the assumption that the scattering electrons are located on the plane of the sky ($z = 0$). In this way, a lower limit estimate of the column density N_e is obtained. However, in their quantitative comparison between the real 3D structure of a flux-rope CME obtained from MHD simulations and that derived via the polarization-ratio technique, Pagano et al. (2015) recently demonstrated that if $B_{\rm exp}$ is calculated by assuming $z = \langle z_{\rm cme}\rangle$ with $\langle z_{\rm cme}\rangle$ center of mass of the LOS plasma distribution, the resulting value of N_e is much closer to the real one, with uncertainties that are generally lower.

An estimate of the location of the emitting plasma along the LOS, $\langle z_{\rm cme}\rangle$, can be obtained with the so-called polarization-ratio technique, first proposed by Moran & Davila (2004) to infer from a single-viewpoint pB image of a CME the three-dimensional structure of the ejected plasma. The degree of polarization introduced by the Thomson scattering is a function of the scattering angle between the incident photon direction and the direction toward the observer (see Billings 1966), and, in turn, of the distance z of the scattering electron from the POS. As shown by Moran & Davila (2004), the dependence of the ratio $p = pB/B = p(z)$ for a single electron on the distance from the plane of the sky can be exploited to determine, pixel by pixel in the CME image, the mean position $\langle z_{\rm cme}\rangle$ of the CME plasma. The more the region where the electron density is locally increased by the CME is spatially limited along the LOS, the more accurate this determination is (see Bemporad & Pagano 2015). On the other hand, owing to the forward/backward symmetry of the Thomson-scattering process, it is impossible to establish with this method if the emitting plasma is actually located in front of or behind the plane of the sky, because $\langle z_{\rm cme}\rangle$ can be derived aside from its sign. Hence, additional considerations are needed to discriminate between these two possible cases.

A key point in applying the polarization-ratio technique is the coronal background removal, which is necessary to exclude from the observed emission contributions coming from both the surrounding ambient corona and the dust-scattered (F-corona) component that affects the unpolarized part of the total brightness. These contributions, that sum together with the genuine CME emission because of the optical thinness of the solar corona, would result in an erroneous determination of the CME 3D structure.

The background removal is usually performed by subtracting a convenient pre-CME image from the frame that is analyzed; for the polarized visible light, this operation can be achieved in several ways: for instance by subtracting the pre-event Stokes parameters from the Stokes images of the CME, or by subtractig pre-event B and pB images directly from the corresponding B and pB images of the CME (see, e.g., Dere

et al. 2005), or even by subtracting pre-event frames separately from all the polarized images before they are combined to obtain the pB (see Moran & Davila 2004). On the other hand, Mierla et al. (2009) suggested a different approach that consists in subtracting from the exposure containing the CME a minimum-intensity image instead of a single pre-event frame. The minimum-intensity image is created by taking, pixel by pixel, the minimum brightness value over a sequence of exposures acquired before and during the event.

In our analysis, we followed the methods described in Moran & Davila (2004) and Mierla et al. (2009) within certain limitations. As stated above, LASCO-C2 usually acquires one or two sequences of three polarimetric images per day. With this quite poor temporal cadence, the minimum-intensity background image cannot be created with more than one pre-CME exposure, because the configuration of the ambient corona two days before each event can be different from that existing during the CME. For this reason, after standard calibration of the VL images (which includes correction for vignetting and offset bias, and the radiometric calibration; see Llebaria & Lamy 2008, for further details about the LASCO-C2 calibration), we computed a minimum-intensity image (for each orientation of the C2 polarizers: 0°, +60°, and −60°) using the exposures acquired soon before, during, and just after each event. In this way, the removal of steady structures not affected by the transit of the CME, such as streamers, turns out to be better than considering only the pre-event and the event images. In the specific case of Event 3, we also took into account the different calibration of the CME images that were acquired with the "blue" filter of the LASCO-C2 instrument, unlike all the other images considered in this work, which were taken with the "orange" one.

Another issue to be accounted for is the effect of the CME motion between the polarimetric exposures, which can be a source of additional uncertainties in the determination of the polarized brightness because of the partial misalignment between the same CME structures in different images. This is a minor concern in our case, however, because the events analyzed here were slow or very slow CMEs: we estimated that in the worst case (i.e., Event 2, where the maximum projected velocity was ≈250 km s^{-1}) the CME front moved less than 2 pixels between consecutive exposures. In order to compensate for this displacement, and following the same procedure adopted by Moran & Davila (2004), we smoothed each polarized exposure using a 3 pixel by 3 pixel median filter. In this way, information at spatial scales equal or lower than 3 pixels (=71.4 arcsec) is lost, but this also significantly reduces the errors associated with the CME motion.

The polarimetric images were then used to compute the Stokes parameters (I, Q, and U) that were corrected for the small instrumental elliptical polarization produced by the two folding mirrors in the beam path, which was removed with the use of the Müller matrix formalism following the method described in Moran et al. (2006). Finally, the B and pB images of the CME were obtained (see Figure 3, left column) with the standard relationships $B \equiv I$ and $pB \equiv \sqrt{Q^2 + U^2}$ (see Landi Degl'Innocenti & Landolfi 2004). In this way, the radiometric calibration of the polarized exposures is not strictly necessary when applying the polarization-ratio technique, because the ratio pB/B is used to determine the position of the emitting plasma along the LOS; conversely, it is essential for the derivation of the electron density (see below). As explained by Frazin et al. (2012), the uncertainty in the standard radiometric calibration of C2 can be considered reasonably within ±15% of the measured pB and B values, so we used this value for the estimate of the errors associated with all the other derived quantities.

For each pixel in the background-subtracted CME pB image, the mean distance from the POS of the plasma responsible for the emission in that pixel was estimated by comparing the observed ratio $p_{\rm obs}$ with the theoretical ratio $p_{\rm exp}$ expected for a single electron, according to the Thomson-scattering theory. We used the SolarSoft routine `eltheory.pro` to compute the values of $p_{\rm exp}$ for a range of distances z from the POS and found the value $\langle z_{\rm cme}\rangle$ for which $p_{\rm obs} = p_{\rm exp}$. Note that, as shown by Bemporad & Pagano (2015), the resulting $\langle z_{\rm cme}\rangle$ actually represents the location along the LOS of the center of mass of a "folded" density distribution, given by reflecting and summing in front of the POS the fraction of the real density distribution located behind the POS. This leads to over/underestimates of the real distance from the POS of the emitting plasma and the derived $\langle z_{\rm cme}\rangle$ can be considered more accurate only when the emitting plasma is at an angle of ∼20° from the plane of the sky.

The topographical z-maps derived for the three events are shown in Figure 3 (center column) together with the background-subtracted pB maps (filtered using the NRGF filter to highlight the latitudinal structures; left column). Note that the calculation of $\langle z_{\rm cme}\rangle$ was restricted only to pixels with values of pB and B above 10% of the mean, in order to prevent artifacts in the 3D reconstruction.

The map relevant to Event 1 shows that the CME front and core plasma is concentrated at an average distance of ∼1.6 $R_\odot$ from the POS (i.e., at an average angle of ∼30°), while in the regions surrounding the front and in the cavity (the low-brightness region inside the CME) the emission appears to be associated with plasma located at greater distances from the POS. This result can be interpreted in light of what is found by Bemporad & Pagano (2015): the density distribution of the plasma in the void of the CME and in the surrounding quiet regions is most probably extended along the LOS more than that in the front and in the core, which are more spatially confined; therefore, in the former regions, the tail of the density distribution behind the POS is reflected back in front of the POS when the polarization-ratio technique is applied (due to the sign ambiguity of the method, as explained above) and this leads in turn to an overestimate of $\langle z_{\rm cme}\rangle$.

The z-map of Event 2 shows that around 21:00 UT the leading edge of the ejected plasma, located at a heliocentric distance of ∼4.5 $R_\odot$, had correspondingly reached the maximum average distance from the POS of ∼3.5 $R_\odot$, consistent with a blob of plasma travelling in a direction forming an angle of ∼40° from the POS. At lower altitudes, other small-scale structures located approximately along the same direction with respect to the plane of the sky can be recognized in the map. Note that, as in the previous case, the brightest features identifiable in the pB map are located systematically closer to the POS in the z-map.

Concerning Event 3, the CME plasma appears to be located at an average distance of about 1.5 $R_\odot$ from the POS in the southern leg of the front, while at higher distances, >3 $R_\odot$, in the northern one. Note that the southern part of the CME front was mostly superimposed to the pre-event coronal streamer, as evidenced by LASCO total-brightness images, so the difference

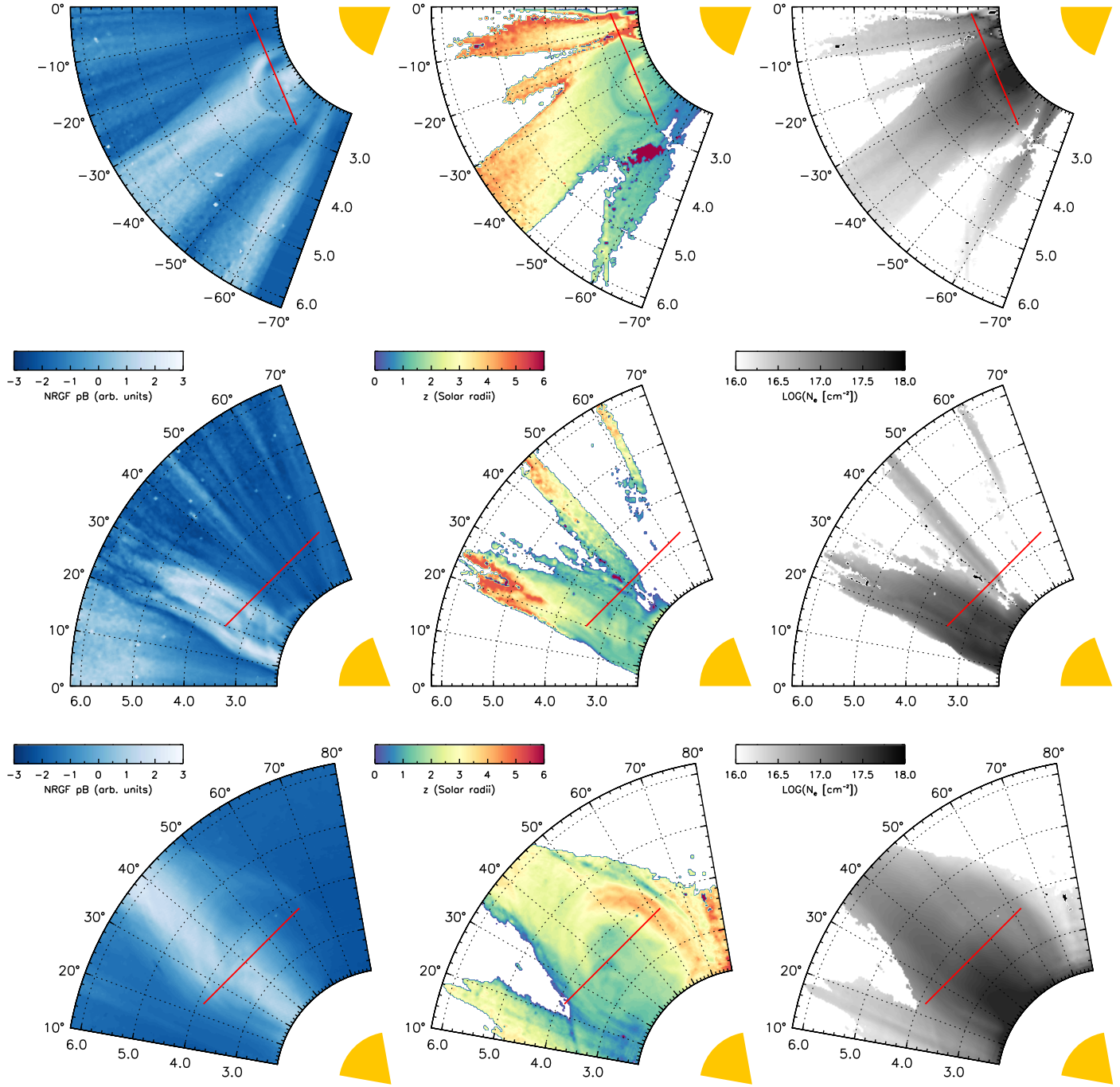

Figure 3. Left column: polar maps (as functions of heliographic latitude and heliocentric distance) of the polarized visible light measured by LASCO-C2 for Event 1 (top row), Event 2 (middle row), and Event 3 (bottom row), after background subtraction and processed with the NRGF. Middle column: topographical maps of the average location along the LOS of the CME plasma, $\langle z_{\rm cme} \rangle$. The white areas correspond to coronal regions excluded from the calculations, as described in the text. Right column: same, for the electron column density N_e derived from the pB. In all panels, the UVCS slit is superimposed as a red line. The solar disk (yellow area) is reported for reference purposes.

in the position along the LOS between the two legs could be due to the contribution of the spurious white-light emission coming from the streamer.

Finally, the resulting z-maps of LOS plasma distribution were used to derive the corrected column density maps (see Pagano et al. 2015), shown in Figure 3 (right column). The column density can be then converted to volume density (units of cm^{-3}) if the thickness L of the CME plasma along the LOS is known; in fact, it is

$$N_e \equiv \int_{\rm los} n_e \, dz \approx \langle n_e \rangle \cdot L, \qquad (2)$$

where $\langle n_e \rangle$ is the average electron density of the CME plasma (see also Quémerais & Lamy 2002, for a discussion on the derivation of electron density maps from the inversion of VL images.). Unfortunately, the parameter L cannot be

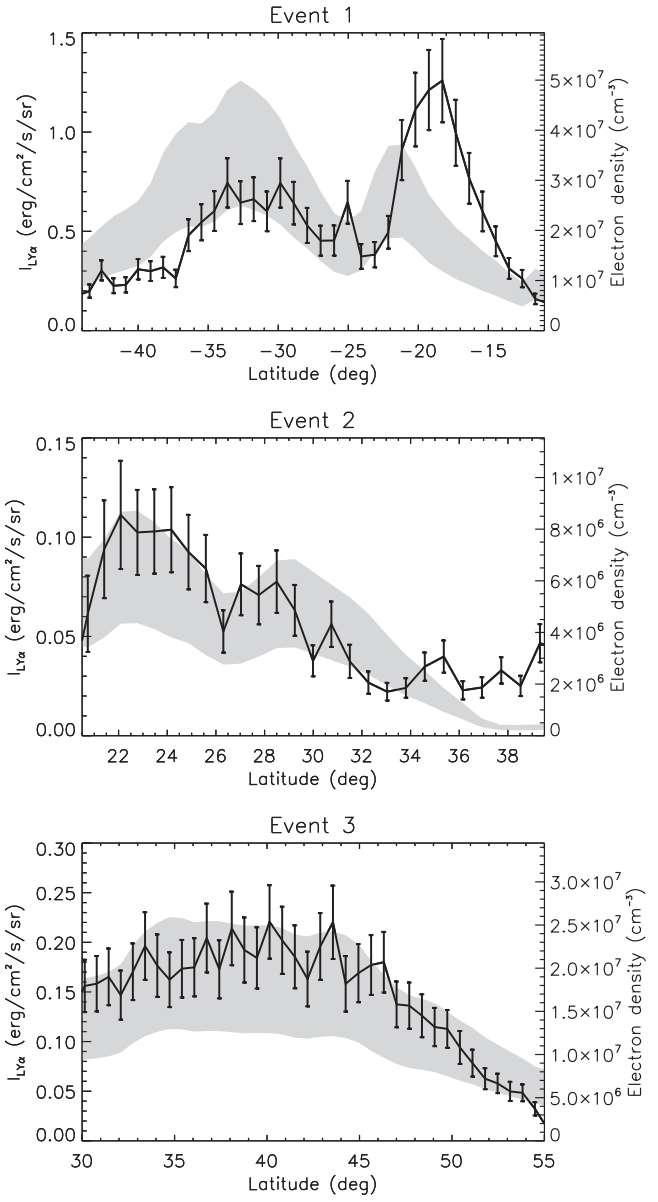

Figure 4. Electron densities (gray shaded areas) and UVCS H I Lyα intensities (heavy line) as functions of the heliographic latitude along the UVCS field of view. Electron densities were derived using two values of the thickness of the CME along the LOS: $L = 0.25\ R_\odot$(upper edge of the shaded area) and $L = 0.5\ R_\odot$(lower edge), as described in the text.

directly estimated from VL images, nor derived with the polarization-ratio technique, but it must be reasonably assumed. For each of our events, we derive the average electron density assuming for L the two values of 0.25 and $0.5\ R_\odot$. We report in Figure 4 the density profiles interpolated along the UVCS slit, together with the corresponding Lyα intensity profiles derived with UVCS.

The electron densities obtained in the three cases are quite consistent with those usually measured in the core of CMEs with other techniques ($\sim 10^6$–$10^7\ \mathrm{cm}^{-3}$; see, e.g., Ciaravella et al. 2000, 2001; Dobrzycka et al. 2003; Bemporad et al. 2007). Event 2, which turns out to be the faintest in white light, accordingly exhibits the lowest densities (up to $\sim 8 \times 10^6\ \mathrm{cm}^{-3}$). Event 3 shows a noticeable latitudinal correlation between the distribution of the electron density and that of the Lyα intensity. Conversely, for Events 1 and 2, the locations where the density has local maxima appear to be less correlated with the Lyα intensity peaks, in particular, those located around 29°N for Event 2 and around 20°S for Event 1.

We used the electron densities derived from the analysis of LASCO VL images to evaluate the Lyα line intensities expected along the UVCS FOV in the three cases; comparison with the intensities actually measured by UVCS have been used to constrain possible ranges of electron temperatures of the CME plasma under certain assumptions, as we will discuss in the following.

3.2. Combined Analysis of Visible Light and Lyα UV Radiation

The mechanism of formation of many strong coronal lines in the UV (such as the H I Lyα or the O VI doublet lines) is a combination of radiative and collisional excitations, followed by spontaneous emission. The total intensity of such lines is then the sum of a radiative and a collisional component, $I = I_{\mathrm{rad}} + I_{\mathrm{col}}$. The radiative component is produced by resonant scattering of the chromospheric radiation by coronal ions and can be affected by the outflows of the scattering atoms through the Doppler-dimming effect. We refer the reader to Kohl & Withbroe (1982) and Noci et al. (1987) for a complete treatment of the resonant scattering and Doppler-dimming processes in coronal plasmas.

An approximate expression for the radiative component, holding for coronal structures that are spatially limited along the LOS (e.g., coronal streamers or CMEs; see also Kohl et al. 2006), is

$$I_{\mathrm{rad}} \simeq \frac{h}{16\pi} B_{12} \cdot b \cdot \lambda_0 \cdot \Omega \cdot F_D(v_{\mathrm{out}}) \int_{\mathrm{los}} n_i\, dz, \qquad (3)$$

where h is the Planck constant, B_{12} is the Einstein coefficient for absorption, b is the branching ratio for radiative de-excitation, λ_0 is the wavelength of the line transition, Ω is the solid angle subtended by the solar disk at the scattering location, n_i is the ion number density, and

$$F_D(v_{\mathrm{out}}) = \int_0^\infty I_\odot(\lambda - \delta\lambda)\Phi(\lambda - \lambda_0)d\lambda \qquad (4)$$

is the so-called Doppler-dimming factor, which is a function of the intensity line profile of the chromospheric radiation, $I_\odot(\lambda - \delta\lambda)$—shifted by the quantity $\delta\lambda = (v_{\mathrm{out}}/c) \cdot \lambda_0$, i.e., the Doppler shift introduced by the radial component of the plasma outflow velocity v_{out}—and the normalized coronal absorption profile along the direction of the incident radiation, $\Phi(\lambda - \lambda_0)$.

The collisional component is due to the de-excitation of a coronal ion previously excited by collision with a free electron. Approximately, it is given by

$$I_{\mathrm{col}} \simeq \frac{1}{4\pi} b \cdot q_{\mathrm{col}}(T_e) \int_{\mathrm{los}} n_e \cdot n_i\, dz, \qquad (5)$$

where the term

$$q_{\mathrm{col}}(T_e) = 2.73 \times 10^{-15} \cdot \bar{g} \cdot f_{12} \cdot \frac{1}{E_{12}} \cdot \frac{1}{\sqrt{T_e}} e^{-\frac{E_{12}}{k_B T_e}} \qquad (6)$$

is the collisional excitation rate, which depends on the average Gaunt factor, $\bar{g}$, the oscillator strength of the transition, f_{12}, the

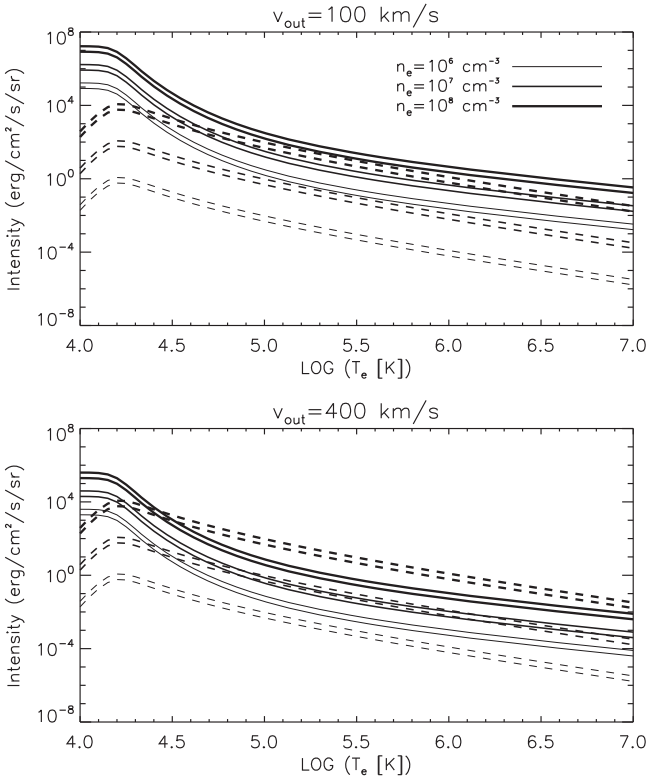

Figure 5. Modeled radiative (solid line) and collisional (dashed line) components of the H I Lyα intensity as functions of the electron temperature T_e, for two representative values of the the plasma outflow velocity (top and bottom panels, respectively), three values of the electron density (marked with different line thickness), and two values of the assumed thickness of the emitting plasma volume along the LOS (the upper line in each couple corresponds to the greater value of L, see the text).

transition energy, $E_{12} = hc/\lambda_0$, and the electron temperature, T_e.

In both Equations (3) and (5), the numerical density of the emitting ions can be approximated using the relationship (see, e.g., Withbroe et al. 1982)

$$n_i \approx 0.83 \cdot A \cdot R(T_e) \cdot n_e, \tag{7}$$

where the factor 0.83 is the ratio of proton to electron density in the case of fully ionized plasma with 90% of H and 10% of He (as in typical coronal plasma conditions), A is the element abundance relative to hydrogen ($A = 1$ for H^0 ions), and $R(T_e)$ is the element ionization fraction, which is a function of the electron temperature. Therefore, if L is the thickness along the LOS of the emitting plasma, the above equations simplify to

$$I_{\rm rad} \propto R(T_e) \cdot F_D(v_{\rm out}) \cdot \langle n_e \rangle \cdot L \text{ and} \tag{8}$$

$$I_{\rm col} \propto R(T_e) \cdot q_{\rm col}(T_e) \cdot \langle n_e \rangle^2 \cdot L. \tag{9}$$

Equations (8) and (9) can be applied to the case of the H I Lyα emission and used to constrain the electron temperature by the excitation rates needed to account for the observed line intensity.

As an example, we report in Figure 5 the prediction of the radiative and collisional components of the H I Lyα intensity as functions of the electron temperature T_e, for two representative values of the the plasma outflow velocity (100 and 400 km s^{-1}), three values of the electron density (10^6, 10^7, and 10^8 cm^{-3}), and two values of the thickness along the LOS ($L = 0.25\ R_\odot$ and $L = 0.5\ R_\odot$). These estimates were made using standard values for all the atomic coefficients and the other quantities entering Equations (8) and (9), and by adopting the ionization equilibrium provided by the CHIANTI atomic database (version 7) for hydrogen. The idea of our analysis is to derive the expected total H I Lyα intensity $I_{\rm exp}(T_e)$, as a function of T_e, given by $I_{\rm exp}(T_e) = I_{\rm rad}(T_e) + I_{\rm col}(T_e)$ and then to determine T_e from a comparison between $I_{\rm exp}(T_e)$ and the real observed intensity.

Nevertheless, the relative importance of radiative and collisional contributions is also related to the plasma outflow speed. For the Lyα transition, the radiative component is usually dominant in coronal plasmas; however, at low velocities, due to the Doppler-dimming effect, it becomes comparable to the collisional one at coronal temperatures (10^5–10^6 K) when the electron density is higher than 10^8 cm^{-3}. At higher velocities, the radiative component is significantly dimmed, and it can be even lower than the collisional one when the electron density exceeds 10^7 cm^{-3}. It is worth noting that the variation of the LOS thickness L of the emitting plasma has a much lower effect on the Lyα intensity than the variation of the outflow velocity and/or the electron density.

Therefore, the determination of CME plasma temperatures requires the constraint of the outflow plasma velocity as well, in order to estimate the Doppler-dimming factor F_D. A first estimate is simply provided by the POS component of the CME speed, $v_{\rm pos}$, measured with LASCO. We used the two consecutive total-brightness exposures acquired before and after the time of the pB measurement, to determine the radial component of the CME front projected on the POS, by locating homologous points along the front at the two different times and computing $v_{\rm pos} = \Delta h/\Delta t$. This allowed us to derive the profile of the radial velocity in different points located along the UCVS slit FOV (i.e., at different latitudes). Nevertheless, the $v_{\rm pos}$ is an underestimate of $v_{\rm out}$ (which is the real radial component of the plasma outflow velocity) because of the projection effect. It is possible to correct for this effect and obtain a better estimate of real $v_{\rm out}$ by using information on the angle φ between the POS and the reconstructed position of a CME plasma element derived with the polarization-ratio technique, owing to the relationship

$$\cos\varphi = \frac{\rho}{\sqrt{\rho^2 + \langle z_{\rm cme} \rangle^2}}. \tag{10}$$

Then, for any position along the UVCS slit, it is $v_{\rm out} = v_{\rm pos}/\cos\varphi$; this also shows how the polarization-ratio technique can be used to derive from single view-points (as those that will be provided with Metis) the real unprojected speed and CME propagation direction, two very important parameters to help constrain the CME propagation time and for Space Weather forecasting purposes.

Once the unprojected velocity has been determined, it can be used to estimate the corresponding Doppler-dimming factor $F_D(v_{\rm out})$; the assumptions we made for the calculation of this parameter (entering Equation (8)) deserve some consideration. The choice of the incident radiation profile from the lower atmosphere, $I_\odot(\lambda)$, is crucial; we adopted here the Lyα disk profile reported by Lemaire et al. (2002) and measured with *SOHO*/SUMER on 2000 November 12, i.e., very close to the dates of Events 1 and 2; note that this profile was reconstructed with a maximum underestimation of 1%, as stated by the authors. We also used the same line profile for Event 3

because, although the integrated Lyα flux may vary by 80% between the solar maximum and minimum (e.g., Tobiska et al. 1997), the spectral line profile does not appear to change significantly over the solar cycle (see Lemaire et al. 2002). The line profile was scaled so that the total integrated line intensity matched the Lyα irradiance measured by the UARS/SOLTICE (Woods et al. 2000) instrument at the times of Events 1 and 2 (5.34×10^{11} and 5.94×10^{11} photons cm^{-2} s^{-1}, respectively) and by the TIMED/SEE instrument at the time of Event 3 (4.70×10^{11} photons cm^{-2} s^{-1}). Note that these values are more than a factor of approximately two higher than the average quiet-Sun Lyα flux reported by Vernazza & Reeves (1978), which is often used as a reference; this difference is consistent with the fact that the value reported in Vernazza & Reeves (1978) was measured during the solar minimum, while our events are close to the maximum.

The absorption profile $\Phi(\lambda - \lambda_0)$ was assumed to be Gaussian with a $1/e$ line width equal to the average Lyα line width measured by UVCS in the three cases. Since the measured line width is actually an upper limit, because of the possible sources of line broadening that have been neglected, the calculated Doppler-dimming factor is underestimated, and this leads in turn to an underestimate of the radiative component of the Lyα line.

Once the Doppler-dimming factors are computed, given the average electron densities derived from LASCO in the specific cases of our events, we evaluated for each position along the UVCS FOV, the radiative and collisional component of the Lyα line for a range of electron temperatures, and obtained the expected total intensity as a function of the temperature, $I_{\rm exp}(T_e)$. We then found, through inspection, the temperature at which the expected intensity matches the observed one. In this way, we determined, at the same time, not only the electron temperatures T_e, but also the relative contributions of the radiative and collisional components needed to reproduce the observed total intensity.

4. RESULTING CME ELECTRON TEMPERATURES

The electron temperature profiles along the UVCS slit for the three events are shown in Figure 6 (blue shaded areas); these temperatures have been computed from the Lyα intensity, with the same technique that will be applied to future Metis images. For comparison, these electron temperatures T_e are compared with the effective temperatures $T_{\rm eff}$ derived from the analysis of the UVCS Lyα spectra as explained in Section 2.2 (red areas). For both temperatures, the width of the shaded areas is equal to the uncertainties affecting the quantities. As mentioned, $T_{\rm eff}$ values should be considered as an upper limit to real hydrogen kinetic temperatures, which is representative, in turn, of the proton temperature T_p. For reference purposes, we also plotted the electron temperature curves derived assuming that the observed Lyα intensity was due to the radiative component alone (the "radiative" approximation; dashed line) and to the collisional component alone (the "collisional" approximation; dotted line). Finally, all the plotted quantities were obtained assuming $L = 0.25\ R_\odot$.

The Lyα effective temperatures $T_{\rm eff}$ are in all cases quite uniform, within the uncertainties, in the considered regions along the UVCS FOV. The average value of $T_{\rm eff} \simeq 10^6$ K is characteristic of coronal conditions. The H I Lyα profile in CME cores is usually narrower than typical coronal profiles and UVCS observations often imply proton temperatures of the order of 10^5 K (Kohl et al. 2006), well below the value derived in this work. These lower temperatures are usually interpreted as a signature of chromospheric plasma embedded in the expanding CME core. However, Bemporad et al. (2007) also found evidence of hydrogen kinetic temperature around 1.6×10^6 K in their analysis of a CME observed by UVCS on 2000 January 31.

The electron temperatures derived in the general case (the blue curves) are in the range of $10^{5.5}$–$10^{6.5}$ K, in agreement with the values typically detected for CMEs. For Events 1 and 3, where it is possible to almost clearly identify the front and the core of the CME along the UVCS slit based on the distribution of both Lyα intensity and electron density (see also Figure 4),

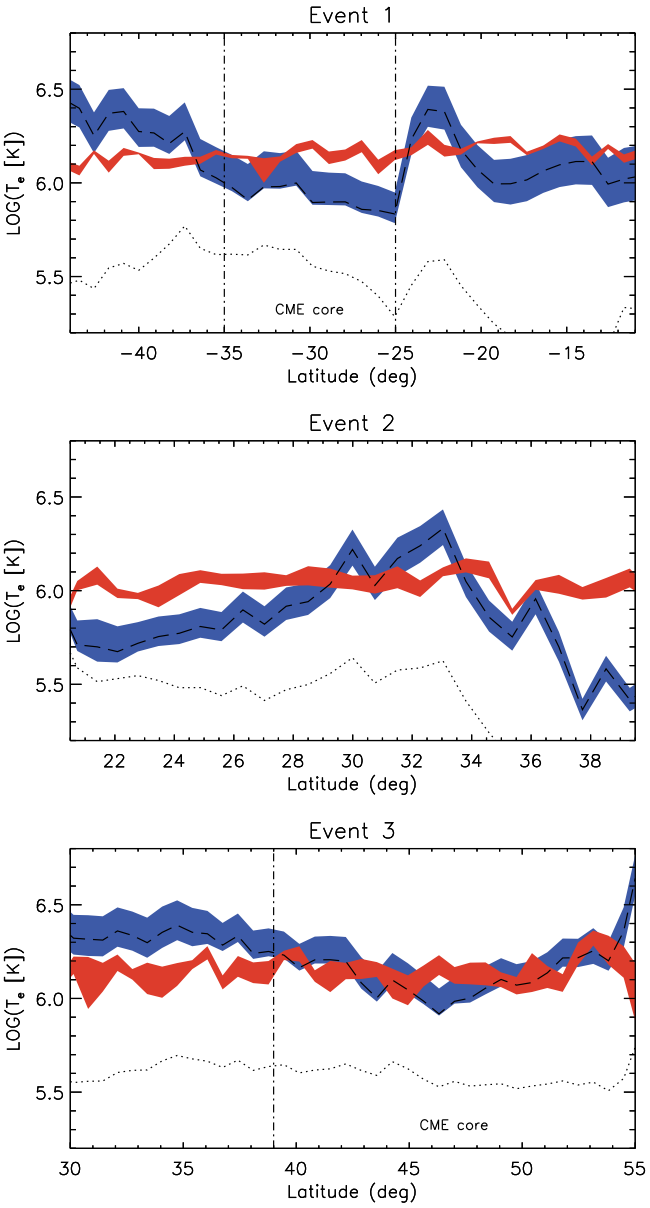

Figure 6. H I Lyα effective temperature derived from UVCS spectra (red shaded area) and electron temperature derived from the analysis described in the text (blue shaded area), as functions of the heliographic latitude along the UVCS field of view. The vertical width of the areas is equal to the uncertainties affecting the results. The dashed and dotted lines represent the electron temperature derived with the radiative and collisional approximations, respectively (see the text). The location of the CME core is indicated in the plots relevant to Events 1 and 3.

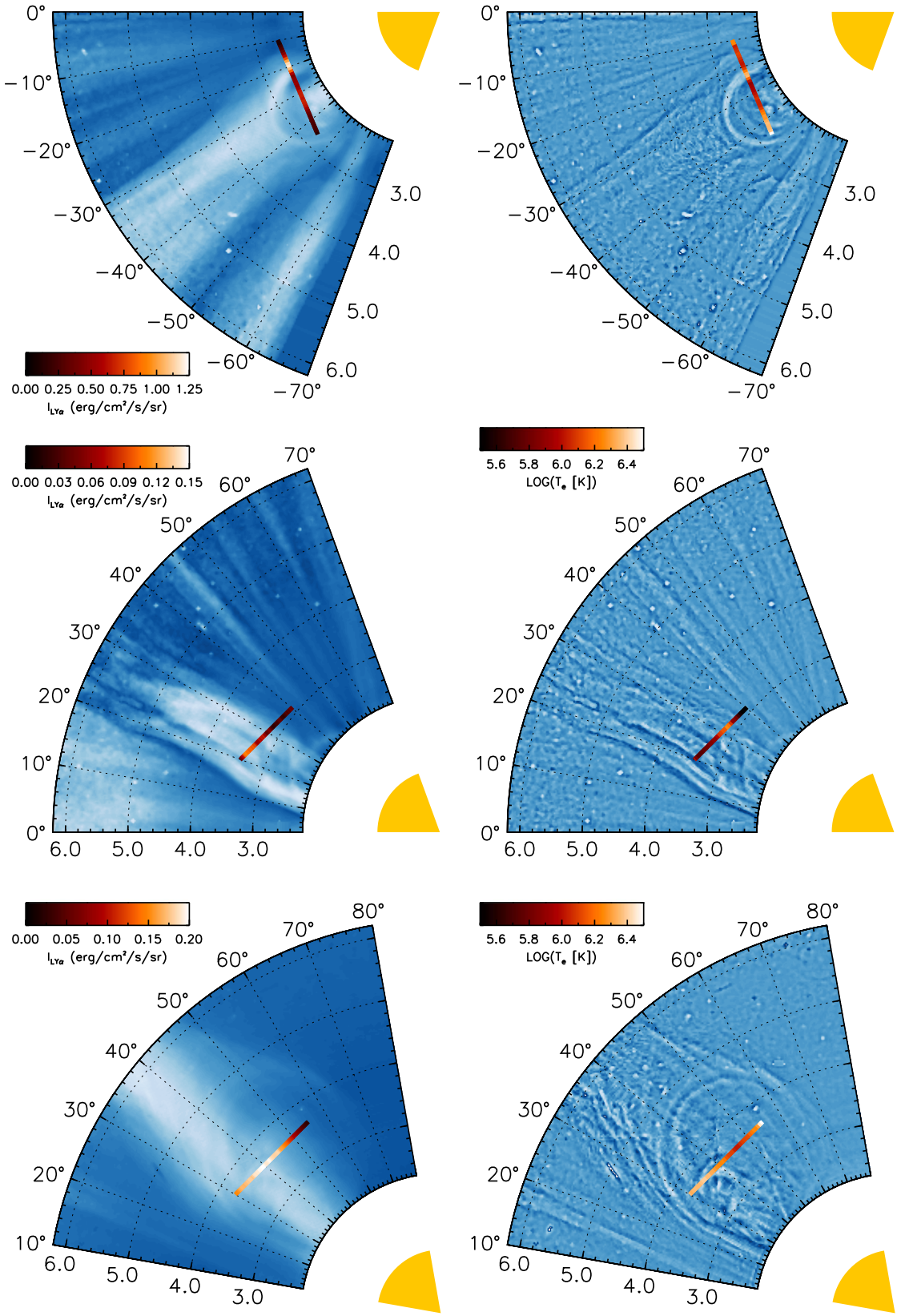

Figure 7. Polar maps (as functions of heliographic latitude and heliocentric distance) of the polarized visible light measured by LASCO-C2 for Event 1 (top row), Event 2 (middle row), and Event 3 (bottom row), processed with the NRGF (left column) and with a filter that highlights emission gradients (right column). The observed H I Lyα intensities and the derived electron temperatures along the UCVS slit are superimposed on the left and right plots, respectively, using color gradients according to the color bars.

the latitudinal variations in the T_e curve reflect the CME structures to some extent. To make evident possible correlations, we plotted in Figure 7 a comparison between the observed Lyα intensities along the UCVS slit superimposed on the LASCO-C2 *pB* intensity images (left column), and a comparison between the derived electron temperatures along the UVCS slit and the same LASCO-C2 *pB* intensity images filtered to highlight emission gradients associated with the CME features (right column).

The comparison shows that, in the first case (Event 1, first row), the electron temperature is lower ($\sim 10^6$ K) in the region corresponding to the core; then, it increases up to $10^{6.5}$ K in the surrounding regions located in the CME front. The core T_e is quite large compared to typical temperatures measured by UVCS in the cores of other CMEs ($10^{4.5}$–$10^{5.5}$ K; see Ciaravella et al. 2000, 2001; Akmal et al. 2001; Kohl et al. 2006), but it is similar to the temperature measured, for instance, by Ciaravella et al. (2003) in the core of a CME observed in 2000. The peak located around -22.5°S is consistent with the position of the CME front and could be interpreted as the signature of heating by plasma compression. The temperature increase below -35°S could be associated with the CME void that is crossed by the UVCS slit: for instance, Ciaravella et al. (2003) have found evidence of $T_e > 10^{6.2}$ K in the void of the same CME mentioned above.

The same correlation can also be recognized in the results of Event 3, though the variations of the electron temperature with latitude are less pronounced in this case. At latitudes around 30°N the UVCS slit crosses the front of the CME (see Figure 7, bottom panels) and correspondingly the electron temperature is higher at those latitudes ($T_e \simeq 10^{6.3}$ K); then, it decreases in the regions identifiable as the core of the CME (above 40°N, where $T_e \approx 10^6$ K). Even in this case we get temperatures quite higher than typical values reported in the literature.

Event 2 is quite peculiar because it does not consist of a classical CME, as described in Section 2.1; thus, it is not possible to identify a core or a front region. However, the steep increase of the electron temperature from $\sim 10^{5.7}$ K at 22°N to $10^{6.3}$ K at 33°N is an indication of the different plasma conditions sampled by the UVCS slit. The southern edge of the slit is superimposed on the ejected blob, as is evident from Figure 7 (middle panels), which most probably consists of plasma at chromospheric temperatures ($\sim 10^5$ K) coming from lower layers of the Sun's atmosphere; as the latitude increases, the slit progressively samples the quiet regions surrounding the blob, which likely have higher temperatures, closer to typical coronal values of $\sim 10^6$ K. Note that the sudden decrease of T_e above $\sim$33°N is due to an analogous decrease of the electron density (see Figure 4) caused by background-subtraction effects, and it could not necessarily imply a real trend.

A comparison of the temperature curves derived and the radiative and the collisional approximations (Figure 6, dashed and dotted lines respectively) shows that in all three cases the contribution of the radiative component to the observed Lyα intensity is overwhelming. This is not surprising, considering that at the quite low velocities characteristic of our events ($v_{\rm out} < 250$ km s^{-1} in all cases) a non-negligible fraction ($\sim$20%) of the radiative component survives the Doppler-dimming effect. The electron temperatures derived with the collisional approximation, conversely, are very low, around $\sim 10^{5.5}$ K at most. They are closer to the T_e derived in the general case in the cores of Events 1 and 3 and in the center of the ejected blob of Event 2, but in any case they are a factor of $\sim$2–3 lower. These low values could be the result of an underestimate of the electron density: higher densities would in fact produce a greater collisional component (see Figure 5) and, in turn, higher temperatures would be necessary to reproduce the same observed intensity. However, in our analysis, the electron density is constrained by the column density derived from the visible light (through Equation (2)); to obtain greater values of $\langle n_e \rangle$, we should reduce the value of L; nevertheless, an extension of the CME structures along the LOS lower than $0.25\,R_\odot$ is quite unrealistic (this value is already four times lower than the typical assumption of $L = 1\,R_\odot$ usually done in similar calculations). Note that, since the radiative component depends directly on the electron column density, the choice of the value of L does not substantially affect our final results in the general case.

Finally, as far as the effective temperatures derived from UVCS Lyα spectra can be considered as an indication of the H I kinetic temperatures, our results suggest that electron temperatures are quite comparable with hydrogen temperatures, in particular, in the regions where the former are lower.

5. DISCUSSION AND CONCLUSIONS

In this work, we demonstrate how future observations of CMEs that will be provided by the Metis coronagraph on board the Solar Orbiter will be analyzed to infer physical parameters of the plasma involved in the eruption and to derive, in particular, the electron temperature of the ejected gas. To this end, we first selected eruptive events observed at the same times and at the same coronal locations both in LASCO-C2 polarized-brightness images, and in the UV H I Lyα line by UVCS; it turns out that over the whole era of UVCS, only three events were sampled by both instruments. Then, we analyzed VL data and showed that they can be used to derive not only the electron column density and volumetric density inside the CME, but also the average location of the emitting plasma along the LOS. This in turn can be used, on the one hand, to better constrain the plasma electron densities, and on the other hand, to measure the CME propagation direction with respect to the POS and to derive the unprojected CME speed at different latitudes (i.e., along the UCVS slit).

The unprojected speeds can be converted into Doppler-dimming factors, the missing ingredient needed to combine VL with UV intensities. Given the electron densities and Doppler-dimming factors, the combination of VL and UV intensities provides an estimate of CME plasma electron temperatures. As we showed here, for the three events we selected, the unprojected speeds were so small that the Lyα emission is still dominated by the radiative component. Nevertheless, we expect that, for major and faster CMEs, the situation could be reversed, with the Lyα emission being dominated by the collisional component, in particular, in the denser parts such as the CME cores. In this work, we found that the CME cores are usually associated with cooler plasma, and that a significant rise of temperatures is observed moving from the core to the front of the CME.

The determination of electron temperatures inside CMEs is of crucial importance. In fact, one of the main problems left open after the UVCS era is the real evolution of the CME thermal energy during their expansion. Different authors found that during the expansion additional heating sources need to be considered in order to reproduce the observed UV emission,

with heating rates that are comparable (Akmal et al. 2001; Murphy et al. 2011) or even larger (Lee et al. 2009; Landi et al. 2010) than kinetic and potential energies carried by the CME. Furthermore, Bemporad et al. (2007) demonstrated with the only existing multi-slit study of a CME based on UVCS data, that the CME plasma temperature is increasing during the expansion, implying again the existence of an additional thermal-energy source. The same results have recently been confirmed by Lee et al. (2015) using *Hinode*/XRT images. Nevertheless, thus far, a clear interpretation of the source of this additional thermal energy is missing.

In this work, we demonstrate how CME electron temperatures can be derived using VL images and UV Lyα intensities. Nevertheless, being limited here to the one-dimensional FOV of the UVCS slit and to the single time when both VL *pB* and UV Lyα emissions were observed, it was neither possible to study the CME plasma temperature distribution within the whole CME bubble, nor its time evolution during the CME expansion. A full investigation of these aspects will be possible thanks to future data that will be provided by the Metis coronagraph on board the Solar Orbiter. In fact, sequences of VL and UV images that will be acquired at the same time, will allow us to study both the thermal-energy distribution within the CME bubble at a given time, and its evolution during the CME propagation. Further analysis on the kinematics and 3D structure of CMEs will also be possible thanks to the synergies between Metis and other next-generation coronagraphs, such as ASPIICS (Renotte et al. 2015) on board the ESA Proba-3 mission. Moreover, for events that will be observed during quadratures also by other spacecrafts (such as Solar Probe Plus), the combination of this information with in situ measurements made close to the Sun will allow us to tightly constrain the temporal evolution of thermal energy of the ejected plasma during its early interplanetary propagation, thus letting connections with the still open issue of in situ detections of high-ionization states of heavy ions in interplanetary CMEs.

The work of R.S. has been funded by the Agenzia Spaziale Italiana through contracts ASI/INAF N. I/013/12/0 and I/013/12/0-1. Mauna Loa Mark-IV data are courtesy of the Mauna Loa Solar Observatory, operated by the High Altitude Observatory, as part of the National Center for Atmospheric Research (NCAR). NCAR is supported by the National Science Foundation. *SOHO* is a mission of international cooperation between ESA and NASA.

REFERENCES

Airapetian, V. S., & Usmanov, A. V. 2016, ApJL, 817, L24
Akasofu, S.-I. 2011, SSRv, 164, 85
Akmal, A., Raymond, J. C., Vourlidas, A., et al. 2001, ApJ, 553, 922
Antonucci, E., Fineschi, S., Naletto, G., et al. 2012, Proc. SPIE, 8443, 844309A
Bemporad, A., Mierla, M., & Tripathi, D. 2011, A&A, 531, A147
Bemporad, A., & Pagano, P. 2015, A&A, 576, A93
Bemporad, A., Raymond, J. C., Poletto, G., & Romoli, M. 2007, ApJ, 655, 576
Bemporad, A., Soenen, A., Jacobs, C., et al. 2010, ApJ, 718, 251
Bemporad, A., Susino, R., & Lapenta, G. 2014, ApJ, 784, 102
Billings, D. E. 1966, A Guide to the Solar Corona (New York: Academic Press)
Brueckner, G. E., Howard, R. A., Koomen, M. J., et al. 1995, SoPh, 162, 357
Byrne, J. P., Maloney, S. A., McAteer, R. T. J., et al. 2010, NatCo, 1, 74
Ciaravella, A., Raymond, J. C., Kahler, S. W., et al. 2005, ApJ, 621, 1121
Ciaravella, A., Raymond, J. C., Reale, F., Strachan, L., & Peres, G. 2001, ApJ, 557, 351
Ciaravella, A., Raymond, J. C., Thompson, B. J., et al. 2000, ApJ, 529, 575
Ciaravella, A., Raymond, J. C., van Ballegooijen, A., et al. 2003, ApJ, 597, 1118
Dere, K. P., Wang, D., & Howard, R. 2005, ApJL, 620, L119
Dobrzycka, D., Raymond, J. C., Biesecker, D. A., et al. 2003, ApJ, 588, 586
Farrugia, C. J., Jordanova, V. K., Thomsen, M. F., et al. 2006, JGRA, 111, 11104
Fineschi, S., Antonucci, E., Naletto, G., et al. 2012, Proc. SPIE, 8443, 84433H
Frazin, R. A., Vásquez, A. M., Thompson, W. T., et al. 2012, SoPh, 280, 273
Gurnett, D. A., Kurth, W. S., Stone, E. C., et al. 2015, ApJ, 809, 121
Heinzel, P., Susino, R., Jejčič, S., et al. 2016, A&A, 589, A128
Hultqwist, B. 2008, JASTP, 70, 2235
Iju, T., Tokumaru, M., & Fujiki, K. 2014, SoPh, 289, 2157
Isavnin, A., Vourlidas, A., & Kilpua, E. K. J. 2014, SoPh, 289, 2141
Kay, C., Opher, M., & Evans, R. M. 2013, ApJ, 775, 5
Kohl, J. L., Esser, R., Gardner, L. D., et al. 1995, SoPh, 162, 313
Kohl, J. L., Noci, G., Cranmer, S. R., & Raymond, J. C. 2006, A&ARv, 13, 31
Kohl, J. L., & Withbroe, G. L. 1982, ApJ, 256, 263
Landi, E., Raymond, J. C., Miralles, M. P., & Hara, H. 2010, ApJ, 711, 75
Landi Degl'Innocenti, E., & Landolfi, M. 2004, Polarization in Spectral Lines (Dordrecht: Kluwer)
Lee, J.-Y., Raymond, J. C., Ko, Y.-K., & Kim, K.-S. 2009, ApJ, 692, 1271
Lee, J.-Y., Raymond, J. C., Reeves, K. K., et al. 2015, ApJ, 798, 106
Lemaire, P., Emerich, C., Vial, J.-C., et al. 2002, in From Solar Min to Max: Half a Solar Cycle with SOHO, ed. A. Wilson (Noordwijk, Netherlands: ESA Publications), 508, 219
Llebaria, A., & Lamy, P. 2008, Proc. SPIE, 7010, 70101I
Lockwood, J. A. 1971, SSRv, 12, 658
Mierla, M., Inhester, B., Marqué, C., et al. 2009, SoPh, 259, 123
Moran, T. G., & Davila, J. M. 2004, Sci, 305, 66
Moran, T. G., Davila, J. M., Morrill, J. S., Wang, D., & Howard, R. 2006, SoPh, 237, 211
Möstl, C., Rollett, T., Frahm, R. A., et al. 2015, NatCo, 6, 7135
Murphy, N. A., Raymond, J. C., & Korreck, K. E. 2011, ApJ, 735, 17
Noci, G., Kohl, J. L., & Withbroe, G. L. 1987, ApJ, 315, 706
Pagano, P., Bemporad, A., & Mackay, D. H. 2015, A&A, 582, A72
Quémerais, E., & Lamy, P. 2002, A&A, 393, 295
Raymond, J. C., & Ciaravella, A. 2004, ApJL, 606, L159
Renotte, E., Alia, A., Bemporad, A., et al. 2015, Proc. SPIE, 9604, 96040A
Susino, R., Bemporad, A., & Dolei, S. 2014, ApJ, 790, 25
Susino, R., Bemporad, A., & Mancuso, S. 2015, ApJ, 812, 119
Temmer, M., Rollett, T., Möstl, C., et al. 2011, ApJ, 743, 101
Thompson, W. T., Kliem, B., & Török, T. 2012, SoPh, 276, 241
Tobiska, W. K., Pryor, W. R., & Ajello, J. M. 1997, GeoRL, 24, 1123
Vernazza, J. E., & Reeves, E. M 1978, ApJS, 37, 485
Vourlidas, A., Subramanian, P., Dere, K. P., & Howard, R. A. 2000, ApJ, 534, 456
Withbroe, G. L., Kohl, J. L., Weiser, H., & Munro, R. H. 1982, SSRv, 33, 17
Woods, T. N., Tobiska, W. K., Rottam, G. J., & Worden, J. R. 2000, JGR, 105, 27217
Wu, C.-C., Fry, C. D., Dryer, M., et al. 2007, AdSpR, 40, 1827